Wafer-scale synthesis of monolayer WS₂ for high-performance flexible photodetectors by enhanced chemical vapor deposition

Changyong Lan[1,2], Ziyao Zhou[1,3], Zhifei Zhou[2], Chun Li[2], Lei Shu[1,3], Lifan Shen[3,4], Dapan Li[1,3], Ruoting Dong[1], SenPo Yip[1,3,4], and Johnny C. Ho[1,3,4,5] (✉)

[1] *Department of Materials Science and Engineering, City University of Hong Kong, Hong Kong 999077, China*

[2] *School of Optoelectronic Information, University of Electronic Science and Technology of China, Chengdu 610054, China*

[3] *Shenzhen Research Institute, City University of Hong Kong, Shenzhen 518057, China*

[4] *State Key Laboratory of Millimeter Waves, City University of Hong Kong, Kowloon, Hong Kong 999077, China*

[5] *Centre for Functional Photonics, City University of Hong Kong, Kowloon, Hong Kong 999077, China*

ABSTRACT

Two-dimensional (2D) nanomaterials have recently attracted considerable attention due to their promising applications in next-generation electronics and optoelectronics. In particular, the large-scale synthesis of high-quality 2D materials is an essential requirement for their practical applications. Herein, we demonstrate the wafer-scale synthesis of highly crystalline and homogeneous monolayer WS₂ by an enhanced chemical vapor deposition (CVD) approach, in which precise control of the precursor vapor pressure can be effectively achieved in a multi-temperature zone horizontal furnace. In contrast to conventional synthesis methods, the obtained monolayer WS₂ has excellent uniformity both in terms of crystallinity and morphology across the entire substrate wafer grown (e.g., 2 inches in diameter), as corroborated by the detailed characterization. When incorporated in typical rigid photodetectors, the monolayer WS₂ leads to a respectable photodetection performance, with a responsivity of 0.52 mA/W, a detectivity of 4.9×10^9 Jones, and a fast response speed (< 560 μs). Moreover, once fabricated as flexible photodetectors on polyimide, the monolayer WS₂ leads to a responsivity of up to 5 mA/W. Importantly, the photocurrent maintains 89% of its initial value even after 3,000 bending cycles. These results highlight the versatility of the present technique, which allows its applications in larger substrates, as well as the excellent mechanical flexibility and robustness of the CVD-grown, homogenous WS₂ monolayers, which can promote the development of advanced flexible optoelectronic devices.

Address correspondence to johnnyho@cityu.edu.hk

1 Introduction

Two-dimensional (2D) nanomaterials with strong intramolecular covalent bonds and weak intermolecular van der Waals interactions are widely considered as promising active materials for next-generation electronic and optoelectronic devices [1–3]. More importantly, because of the weak van der Waals forces between layers, it is possible to obtain atomically thin 2D materials with strong interlayer quantum confinement effects, contributing to the extraordinary optoelectronic performance of the corresponding fabricated devices [4]. In particular, the discovery of monolayer graphene has triggered extensive investigations of 2D materials for various optoelectronic devices [5]. Even though graphene exhibits several excellent properties, including high carrier mobility and wide-band absorption spectrum, its zero bandgap inevitably limits its utilization in digital electronics and optoelectronics [6]. Fortunately, a wide variety of 2D materials are currently available, providing an excellent basis to guide the selection of suitable systems [1–4, 6]. For instance, semiconducting transition metal dichalcogenides (TMDCs) are complementary to graphene, and exhibit suitable band gaps of 1–2 eV [6–10]. Among typical TMDCs, WS_2 has a high optical absorption coefficient of 10^5–10^6 cm^{-1} [11], a layer-dependent band gap of 1.3–2.05 eV [12], and large exciton binding energies of 700–800 meV [13, 14]. Theoretical calculations also revealed that the room temperature phonon-limited electron mobility of monolayer WS_2 can be as high as 1,103 $cm^2/(V \cdot s)$ [15].

At the same time, owing to their atomically thin nature and strong in-plane covalent bonding, 2D materials are inherently flexible; this feature makes them highly suitable as active channel materials for applications in mechanically flexible electronics and optoelectronics [16]. In particular, Chang et al. obtained high-performance and highly bendable MoS_2 transistors integrated with high-k dielectrics on flexible substrates [17]. Pu et al. fabricated highly flexible and extremely efficient complementary inverters utilizing large-area TMDC monolayer materials [18]. In addition, flexible photodetectors based on MoS_2 exhibited adequate performance and good mechanical robustness [19]. These features make TMDCs, and WS_2 in particular,

attractive alternatives to graphene in various electronic and optoelectronic applications.

Interestingly, in the early investigations on 2D materials, mechanical exfoliation was often used to isolate the 2D materials from their bulk counterparts, which represented a suitable approach to study the fundamental properties of 2D materials [20–22]. However, practical applications, particularly in electronics and optoelectronics, require the wafer-scale synthesis of atomically thin WS_2 layers with good uniformity. In this regard, chemical vapor deposition (CVD) is extensively employed for the growth of large-area, homogeneous monolayer 2D thin films, and has been successfully applied also to prepare other kinds of 2D materials [23, 24]. In general, monolayer graphene can be readily obtained in large scale by Cu-catalyzed CVD growth [23]. Wafer-scale synthesis of MoS_2 films can also be achieved by the enhanced CVD method [25]. Various groups have attempted to synthesize WS_2 films via different CVD techniques [26–32]. In particular, Zhang et al. achieved the growth of monolayer WS_2 with large grain size (up to several tens of micrometers) on sapphire substrates [29]. By sandwiching a small amount of WO_3 powder between two SiO_2/Si substrates, Cong et al. realized the synthesis of large single-domain WS_2 monolayers, with size exceeding 100 μm [30]. Recently, it was also found that ultra-large single-domain WS_2 (up to hundreds of micrometers) could be obtained by using gold foil as the substrate, since the 2D grain growth is substantially enhanced by the more efficient packing of the adsorbed components, owing to the limited solubility of the precursors (i.e., W and S) in gold [26, 27]. Seed- and halide-assisted CVD schemes have also been tested for the growth of large-area and large-domain monolayer WS_2 [31, 32]. In any case, the wafer-scale synthesis of atomically thin and homogeneous WS_2 with excellent crystallinity still represents a major challenge in the field.

Multi-zone horizontal furnaces have been widely employed for the synthesis of one-dimensional materials, such as III-V semiconductor nanowires [33, 34]. However, so far not many studies have focused on the growth of 2D materials utilizing multi-zone furnaces. Compared with the single-zone furnace, the multi-zone one allows a more effective control on

the precursor evaporation and material deposition processes; therefore, in principle, the multi-zone horizontal furnace would be more suitable for synthesizing high-quality, large-scale, and uniform 2D materials. Herein, we design and demonstrate the growth of wafer-scale and monolayer WS_2 films with high crystallinity using a three-zone horizontal furnace. The versatile control of the evaporation and deposition temperatures in different zones allows obtaining highly crystalline, large-area, homogeneous, and atomically thin WS_2. Upon incorporating these WS_2 monolayers in large-area photodetectors on rigid substrates, impressive on/off current ratios of more than 5.5×10^3, as well as excellent response rates with rise and decay times shorter than 560 μs, were obtained with a 532 nm laser. Moreover, when the WS_2 monolayers were used in mechanically flexible substrates, enhanced photoresponsivities of more than 5 mA/W were achieved. Another interesting finding is that the photocurrent (I_P) increased with decreasing bending radius, which can be attributed to the reduction in the band gaps of the WS_2 monolayers due to compressive stress. More importantly, the photocurrent remains rather stable, with a decay of only 11% even after 3,000 bending cycles. These results clearly highlight the versatility of the present synthesis method based on a multi-zone furnace, along with the technological potential of large-scale and homogeneous monolayer WS_2 films for high-performance optoelectronics. In future, we expect that the improved CVD technique illustrated in this work will also be applicable to the wafer-scale synthesis of other types of 2D materials.

2 Experimental

In this work, as illustrated in Fig. 1(a), a three-temperature-zone horizontal furnace and a quartz tube (1 inch in diameter) were employed for the wafer-scale synthesis of monolayer WS_2 films. In particular, WO_3 powder samples (200 mg, 99% purity, Lanhua Reagent, Tianjin, China) were placed in a quartz boat located at the center of zone 1, while the zone temperature was set to 920 °C. Zone 2 was then employed as the deposition chamber, in which [0001]-oriented sapphire wafers (single-side polished) were used as the growth substrates, while the deposition temperature was fixed
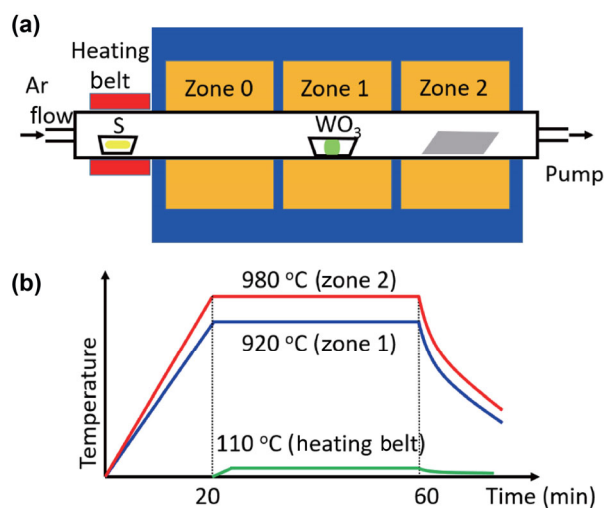

Figure 1 Schematic illustration of the experimental CVD setup based on the three-zone horizontal furnace. (a) Configuration of the experimental setup. (b) Temperature vs. time profiles in different heating zones.

at 980 °C. Sulfur powders (300 mg, reagent grade, 100 mesh, Sigma-Aldrich) were utilized as the sulfur precursor of WS_2. Moreover, since zone 0 was adjacent to zone 1, the accuracy of the temperature control of zone 0, especially in the low-temperature range, would always be affected by the relatively high temperature of zone 1, due to the insufficient thermal insulation of the individual zones in typical horizontal tube furnaces. For instance, when zone 1 reached the preset temperature of 920 °C, although zone 0 is intended to remain fixed at room temperature without supplying any power, its actual temperature would exceed 200 °C, which is not appropriate for the controllable evaporation of the low-vapor pressure sulfur precursor. For this reason, zone 0 was purposely set idle during the synthesis and the sulfur powders, placed in a boron nitride crucible, were heated by a heating belt outside zone 0, with the temperature monitored by an external thermocouple. In this way, the entire zone 0 was used as thermal insulator, to ensure the well-controlled and uniform evaporation of sulfur at 110 °C in the heating belt region.

Before heating, the base pressure of the tube was pumped down to 1×10^{-3} Torr. Argon gas (30 sccm) was introduced in the system during the material deposition, and the pressure was then fixed at 0.16

Torr. The time evolution of the temperature of the different zones is displayed in Fig. 1(b). It is worth mentioning that when a larger quartz tube (e.g., 2 inches in diameter) was employed for the large-area synthesis of monolayer WS_2 films, the evaporation temperature of WO_3 had to be changed to 940 °C in zone 1, while the deposition time was extended to 60 min. After the growth, the system was cooled naturally to room temperature under Ar flow and the color of the substrate turned to light yellow.

For the material characterization and device fabrication, the as-synthesized films were first transferred onto Si/SiO_2 (270 nm thermally-grown oxide) by the well-known surface energy-assisted transfer technique, using polystyrene as the coating material [35]. Then, atomic force microscopy (AFM, diMultimode V, Veeco) was used to evaluate the thickness of the grown WS_2 films. Raman spectroscopy (SR-5001-A-R, Andor) with a 532 nm excitation laser was employed to obtain the Raman and photoluminescence (PL) spectra, as well as the Raman and PL mappings of WS_2. The excitation power was fixed at 2 and 5 mW for the PL and Raman mapping measurements, respectively. Scanning electron microscopy (SEM, G2 Pro, PhenomWorld) was utilized to inspect the surface morphology and homogeneity of the films. An ultraviolet–visible (UV–vis) spectrometer (Lambda 750, Perkin-Elmer) was used to measure the absorption spectrum of the films. For the absorption spectrum measurements, the WS_2 films were transferred on a glass substrate. Transmission electron microscopy (TEM, Tecnai F30, FEI) was also performed to assess the crystal structure and crystallinity of the WS_2 films, after transferring them onto the TEM grids.

At the same time, the electrodes of monolayer WS_2-based field-effect transistors (FETs) fabricated on Si/SiO_2 and photodetectors configured on a sapphire substrate were prepared using a standard lithography process, followed by the deposition of Ti/Au stacks (3 nm/80 nm) using electron-beam evaporation and a lift-off process. When constructed into flexible photodetectors, the monolayer WS_2 films were initially transferred on polyimide (PI) substrates with a thickness of 0.2 mm, followed by the lithography, Ti/Au (3 nm/50 nm) electrode deposition, and lift-off processes. In addition, copper wires (83 μm in diameter) were used as a shadow mask to fabricate flexible photo-

detectors with electrodes of larger size for the mechanical bending tests.

After the device fabrication, the FETs were electrically characterized in a vacuum probe station with a pressure of 5×10^{-5} Torr, while the performance of the photodetectors was evaluated in ambient environment. A 4155C semiconductor analyzer (Agilent Technologies, California, USA) was used as the source and measurement unit, while a 532 nm laser was employed as light source to assess the response of the photodetectors. The laser power was precisely tuned by an attenuator and measured by an optical power meter (PM400, Thorlabs). A home-made mechanical chopper was used to modulate the illumination of the photodetectors.

3　Results and discussion

During the CVD growth, the wafer-scale synthesis of crystalline and homogeneous WS_2 monolayers could be readily achieved by precisely controlling the evaporation temperature of WO_3 (zone 1) and S powders (heating belt region), as well as the deposition temperature (zone 2). The optical image in Fig. 2(a) shows that the growth of monolayer WS_2 can be effectively scaled up to larger substrates using larger quartz tubes. For simplicity, the characterizations of the materials were performed on the monolayer film grown in 1 inch-diameter quartz tubes, unless otherwise noted. AFM measurements were carried out to determine the thickness of the grown WS_2 films. Based on the typical height profile extracted from the samples (Fig. 2(b)), the film thickness is found to be 0.83 nm, in good agreement with the reported thickness of monolayer WS_2 [28–30], confirming that the obtained WS_2 film is grown in monolayer configuration.

Due to optimal light interference, when the monolayer WS_2 is transferred onto Si/SiO_2 (270 nm), the film exhibits a clear optical contrast, compared with the WS_2-free region (Fig. 2(c)) [36]. The homogenous contrast of the film in both optical and SEM images demonstrates the uniformity of the synthesized WS_2 (Figs. 2(c) and 2(d)). To further confirm the uniformity and assess the crystallinity of the monolayer WS_2 film, we performed TEM, high-resolution TEM (HRTEM),
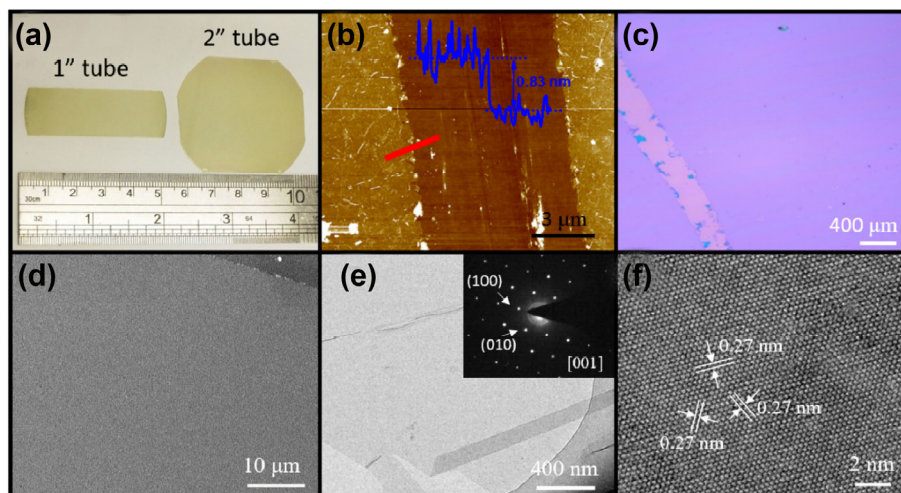
Figure 2 Characterization of the CVD-synthesized monolayer WS_2. (a) Optical image of the wafer-scale monolayer WS_2 synthesized in different quartz tubes (1- and 2-inch in diameter). (b) AFM image of the monolayer WS_2 transferred onto Si/SiO_2 (270 nm) substrates. The scratch was made intentionally before the transfer for identifying the thickness of the obtained film. Inset: height profile along the red line. (c) Optical image of monolayer WS_2 transferred onto Si/SiO_2 (270 nm) substrates. (d) SEM image of monolayer WS_2 grown on sapphire. (e) TEM image of monolayer WS_2. Inset: SAED pattern. (f) HRTEM image of monolayer WS_2.

and selected area electron diffraction (SAED) measurements. A typical TEM image is shown in Fig. 2(e). Except for the folded area, the film displays a consistent contrast, further demonstrating its homogeneity. The excellent crystallinity of monolayer WS_2 is also illustrated by the sharp diffraction spots in the SAED pattern (inset of Fig. 2(e)) and the clear lattice fringes in the TEM image (Fig. 2(f)). Lattice distances of 0.27 nm, corresponding to the {100} planes of WS_2, can also be identified.

Raman spectroscopy is another powerful tool to evaluate the crystal quality and film thickness of 2D materials [37]. A representative Raman spectrum of monolayer WS_2 is shown in Fig. 3(a). The sharp Raman peaks are indicative of the excellent crystallinity of the film, consistent with the TEM results. The corresponding characteristic peaks can also be identified and assigned. In particular, the peak near 355 cm^{-1} can be resolved into three distinct peaks, centered at 345.7, 353.7, and 357.6 cm^{-1}, corresponding to the $E_{2g}^1(M)$, $2LA(M)$, and $E_{2g}^1(\Gamma)$ modes of WS_2, respectively, in perfect agreement with previous reports [30, 38, 39]. Other peaks centered at 298.3, 326.3, and 417.4 cm^{-1} can also be assigned to the $2LA(M) - 2E_{2g}^2(\Gamma)$, $2LA(M) - E_{2g}^2(\Gamma)$, and $A_{1g}(\Gamma)$ modes of WS_2, respectively. The 59.8 cm^{-1} difference between the frequencies of the $E_{2g}^1(\Gamma)$ and $A_{1g}(\Gamma)$

peaks, as well as the absence of the peak near 310 cm^{-1}, point toward the presence of monolayer WS_2 in the samples [30, 40]. Furthermore, as monolayer WS_2 is a direct band gap semiconductor (while multilayer WS_2 is an indirect semiconductor), PL spectroscopy can be used to identify the number of layers in the samples [41]. The as-synthesized WS_2 film exhibits a strong PL emission near 618 nm (Fig. 3(b)), which suggests that it is a monolayer with a band gap of ~ 2 eV, consistent with mechanically exfoliated single-layer WS_2 [41]. Further insight into the optical properties of the synthesized monolayer WS_2 films was obtained by analyzing the UV–vis absorption spectrum of the monolayer. As illustrated in Fig. 3(c), three unique excitonic peaks at 615, 515, and 436 nm are observed in the spectrum, corresponding to A, B, and C excitons, respectively [14]. Peaks A and B are linked to excitonic absorptions in the direct gap of WS_2, located at the K valley of the Brillouin zone. The separation between the A and B peaks is attributed to the splitting of the valence band minimum due to the spin-orbit coupling at the K (K') valley [41]. Peak C is associated with the excitonic transitions from multiple points near the Γ point of the Brillouin zone [41]. Therefore, the excitonic A peak is expected to be correlated with the PL peak, as they have the same origin, and this correlation is perfectly consistent with our results.

The slight difference between the energies of the A and PL peaks can be related to the different substrates employed in the UV–vis and PL measurements, which may affect the excitonic energy [42]. In any case, the energy difference between the excitonic peaks A and C is highly sensitive to the number of layers in WS_2, and this dependence can be utilized to determine the thickness of the WS_2 film [14, 41]. Again, the energy difference between the two excitonic peaks is 0.828 eV, further confirming that the CVD-grown WS_2 is a monolayer film [14]. Raman and PL spectra were also collected in different regions of the as-synthesized substrate (Figs. 3(d) and 3(e)). Combined with the uniform Raman mapping (Fig. 3(f)) and PL mapping (Fig. S1 in the Electronic Supplementary Material (ESM)) images, the nearly identical Raman and PL spectra show the excellent large-area homogeneity of the synthesized monolayer WS_2 film. Overall, these results clearly demonstrate the effective growth of wafer-scale, crystalline, and homogeneous WS_2 monolayers via the simple multi-zone furnace technique presented here, with various potential technological applications.

To shed light on the growth mechanism of the wafer-scale synthesis of monolayer WS_2, we investigated the effect of varying various growth parameters. The quality of the grown WS_2 films is found to be highly sensitive to both the evaporation temperature of WO_3 (zone 1) and the deposition temperature of the substrate (zone 2). For example, placing the growth substrate in position A in zone 1 (Fig. 4(a)) results in a relatively thick WS_2 film with a granular surface (Fig. 4(c)), irrespective of the evaporation temperature there. In contrast, when the substrate is placed in position B in zone 2 (Fig. 4(a)), the morphology and thickness of the grown film are significantly influenced by both the evaporation (zone 1) and deposition (zone 2) temperatures. Using optimal evaporation/deposition temperatures and deposition time, uniform monolayer WS_2 films, similar to the ones depicted in Figs. 2(c)–2(e), can be readily obtained. For relatively short deposition times (e.g., 20 min), discontinuous films are formed, while higher deposition temperatures lead to larger grain sizes. The average grain sizes are determined to be about 300 nm and 2 µm for the films grown at deposition temperatures of 920 and 980 °C, respectively (Figs. 4(d) and 4(e)). In addition, multilayer domain films are observed at higher evaporation temperatures (Fig. 4(f)). In order to understand the effects of the above factors on the crystallinity and morphology of WS_2 films, the fundamental growth process of WS_2 is schematically illustrated in Fig. 4(b).
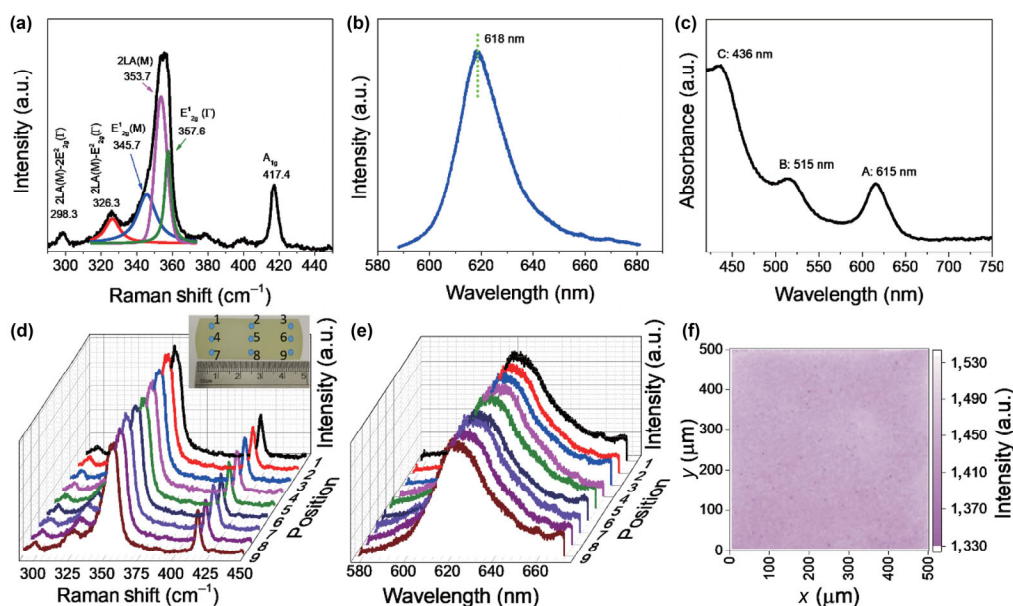

Figure 3 Optical characterization of the monolayer WS_2 film. (a) Raman spectrum. (b) PL spectrum. (c) Absorption spectrum. (d) Raman spectra of the nine different locations marked in the inset. (e) PL spectra of the nine different locations marked in the inset of (d). (f) Raman mapping of the 355 cm^{-1} peak of the monolayer WS_2 film.
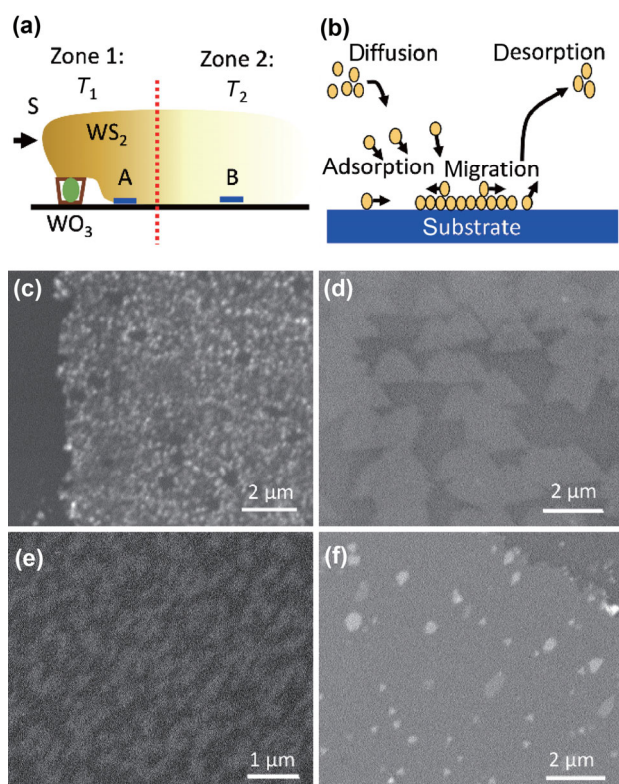
Figure 4 Growth mechanism of the wafer-scale CVD synthesis of monolayer WS_2. (a) Schematic illustration of the precursor vapor distribution established in the horizontal tube furnace. (b) Schematic illustration of the fundamental growth process of monolayer WS_2. SEM images of WS_2 grown under different process conditions: (c) zone 1: 920 °C; (d) zone 1, 920 °C; zone 2: 980 °C, 20 min; (e) zone 1: 920 °C; zone 2: 920 °C, 20 min, and (f) zone 1: 935 °C; zone 2: 980 °C.

Generally, the precursor species are transported from the upstream zone through diffusion and then adsorbed onto the growth substrate, forming WS_2 nuclei. During the growth, the constituent elements of the film remain adsorbed onto the nuclei. Since no dangling bonds in out-of-plane positions are available, the adsorbed elements would have to migrate to the edges of the nuclei, where plenty of dangling bonds are available, giving rise to lateral growth of monolayer WS_2. Inevitably, some adsorbed species would also desorb from the nucleus and leave the substrate in this equilibrium process. Therefore, to achieve continuous and conformal grain growth, the adsorption rate of the WS_2 constituents should be larger than the desorption rate. However, if the deposition temperature is too high, the desorption rate of the WS_2 constituents would become dominant, leading to discontinuous

films with low nuclei density and large grain size (Fig. 4(d)). On the other hand, a low deposition temperature would result in high nuclei density and small grain size (Fig. 4(e)). It is important to note that the CVD synthesis of 2D WS_2 materials is typically controlled by the self-limiting growth mechanism [25]. The partial pressure of the WS_2 constituents must be maintained below certain threshold values to achieve the growth of a homogeneous WS_2 monolayer. If the partial pressures exceed the corresponding thresholds, multilayer growth of WS_2 would be initiated. As a result, multilayer-domain WS_2 films are obtained at a higher evaporation temperature (Fig. 4(f)). When the substrate is placed too close to the precursor source, the high partial pressure of the constituent elements leads to the formation of granular films, due to multilayer nucleation and fast growth rate (Fig. 4(c)). These findings further confirm the importance of reliably controlling various growth parameters for the formation of large-scale, crystalline, and homogeneous WS_2 monolayers by enhanced CVD.

In addition to understanding the growth mechanism of monolayer WS_2, another essential task to assess the potential of these systems in electronic device applications is the analysis of their electrical properties. For this purpose, we fabricated global back-gated FETs based on the obtained monolayer WS_2 (Fig. 5(a) and inset of Fig. 5(b)). The analysis of the output and transfer characteristics shows that the current (I_{ds}) increases with increasing gate voltage (V_{gs}), demonstrating the n-type conductivity of monolayer WS_2 (Figs. 5(a) and 5(b)). Notably, a strong hysteresis is observed for the transfer curves. The occurrence of hysteresis is generally associated with molecules (such as water and oxygen) adsorbed on the surface of WS_2 or at the interface between WS_2 and SiO_2, as well as charge traps such as S vacancies in WS_2, interface traps between WS_2 and SiO_2, and oxide traps in the SiO_2 dielectric [43–45]. The field effect mobility (μ) can be extracted from the transfer curve using the formula

$$\mu = \frac{\partial I_{ds}}{\partial V_{gs}} \cdot \frac{L}{W} \cdot \frac{1}{C_{ox} V_{ds}} \tag{1}$$

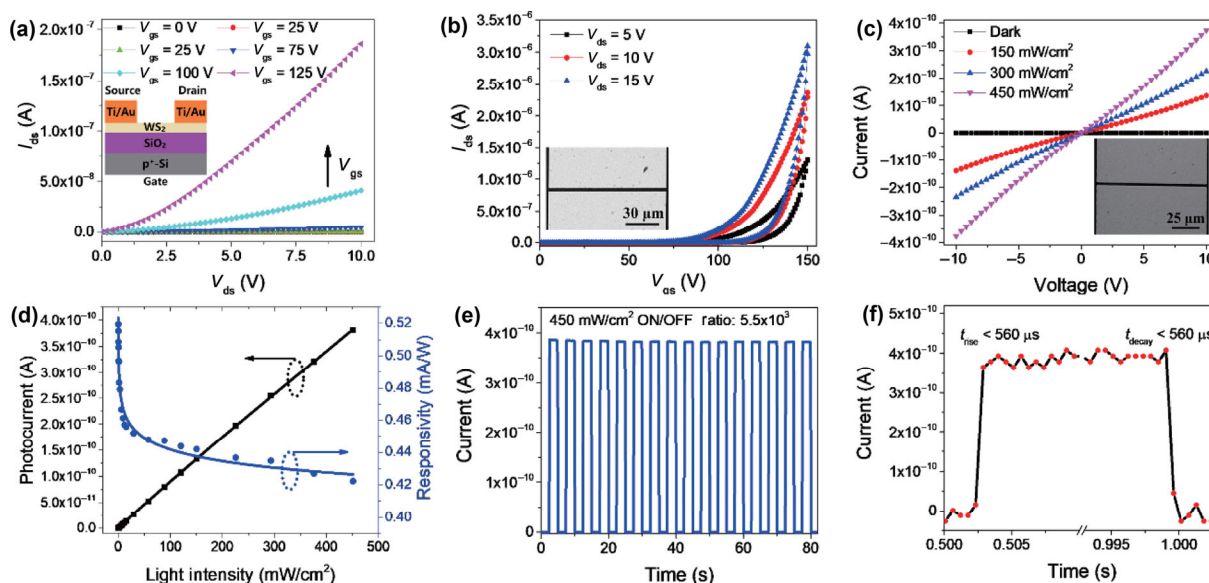where L is the channel length, W is the channel width,

Figure 5 FETs and photodetectors based on WS_2 monolayers. (a) Output characteristics (I_{ds}–V_{ds} curves). Inset: schematic illustration of the FET device structure. (b) Transfer characteristics (I_{ds}–V_{gs} curves). Inset: SEM image of a representative FET. (c) Current vs. voltage plots under different light intensities. Inset: SEM image of a typical photodetector. (d) Photocurrent and responsivity vs. light intensity curves, with a bias voltage of 10 V. (e) Current vs. time plot, with a bias voltage of 10 V under chopped light illumination. (f) High-resolution current vs. time plot, used to illustrate the rise and decay time constants. The device channel length is 2 μm.

C_{ox} is the gate capacitance per unit area, and V_{ds} is the source-drain voltage. The mobility obtained in this way is 0.02 cm²/(V·s), which is relatively small compared with the carrier mobility reported for monolayer WS_2 [26, 27, 31, 32]. Adsorbed molecules, defects in the monolayer WS_2, and trapped charges in the substrate may lead to scattering of electrons, contributing to the low mobility observed for the present sample [45–47]. The relatively low carrier mobility seems to represent a common problem affecting CVD-synthesized large-area TMDCs [25, 48–50]. A large number of defects (such as S vacancies) can be present in the CVD-grown WS_2, and represent the dominating factors limiting the carrier mobility. The performance of the WS_2 transistors is even worse in air, due to the adsorption of large amounts of water and oxygen molecules onto the device channel in ambient environment (Fig. S2 in the ESM). Further work is needed to reduce the defect density of CVD-synthesized WS_2, in order to improve the carrier mobility.

Since monolayer WS_2 is a direct band gap semiconductor, it is interesting to assess the optoelectronic properties of the present wafer-scale samples. To this purpose, photodetectors made of monolayer WS_2 were configured directly on a sapphire substrate (Fig. 5(c), inset). As shown in Fig. 5(c), the detector output current (i.e., photocurrent) increases with the illumination intensity. The photocurrent is defined as the difference between the currents measured under illumination and in the dark. The photocurrent is plotted as a function of the light intensity in Fig. 5(d), where a nearly linear dependence is observed. The curve can be fitted using the formula

$$I_p = A\Phi^\beta \tag{2}$$

where A and β are fitting parameters, and Φ is the light intensity. The β parameter was determined to be 0.961, indicating a low density of charge traps in the monolayer WS_2. The responsivity (R) is another figure of merit used to evaluate the performance of the photodetector, defined as

$$R = \frac{I_p}{\Phi} \tag{3}$$

According to the above equations, R should be proportional to $\Phi^{\beta-1}$, as shown in Fig. 5(d). The largest

R obtained for the present devices was 0.52 mA/W. Moreover, the specific detectivity (D^*) represents the sensibility of the detector towards a weak optical signal. Assuming that the main contribution to the total noise comes from the shot noise from the dark current, D^* can be expressed as

$$D^* = R\sqrt{\frac{S}{2qI_{dark}}} \qquad (4)$$

where S is the effective photo-sensing area of the detector, q is the absolute value of the electron charge, and I_{dark} is the dark current. According to Eq. (4), D^* is proportional to R, leading to the same trend with increasing light intensity (Fig. S3(a) in the ESM). The maximum D^* is estimated to be 4.9×10^9 Jones, for an incident light intensity of 0.07 mW/cm^2. To explore the dynamic behavior of the photodetector, the current can be collected as a function of time when the device is illuminated with chopped light, as shown in Fig. 5(e). It is clear that the current rises and falls during on/off switches, with good stability. A current on/off ratio of 5.5×10^3 is obtained when the light intensity is 450 mW/cm^2. It is also important to evaluate the rise and decay characteristics of the current; for this purpose,

the measured high-resolution current–time curve is shown in Fig. 5(f). The times required for the current to increase from 10% to 90% of the peak value or vice versa define the rise and decay time constants, respectively. No gradual current increase and decay are observed when the light is switched on and off, indicating that the rise and decay time constants of the device are smaller than 560 µs, which is the resolution limit of our instrument. To the best of our knowledge, these are the best values reported for monolayer WS$_2$-based photodetectors to date [32, 51–53]. These results illustrate the impressive performance and promising potential of the present wafer-scale monolayer WS$_2$ for highly efficient photodetection applications.

As mentioned before, as 2D WS$_2$ materials have excellent mechanical flexibility, they are ideal candidates for use in flexible optoelectronics. Nevertheless, only very few reports on flexible WS$_2$ photodetectors have been published. Therefore, we also investigated high-performance and flexible photodetectors based on monolayer WS$_2$ fabricated on PI substrates (Fig. 6(a) and inset of Fig. 6(b)). The current rises upon illuminating the device, and further increases with increasing light intensity (Fig. 6(a)). The photocurrent
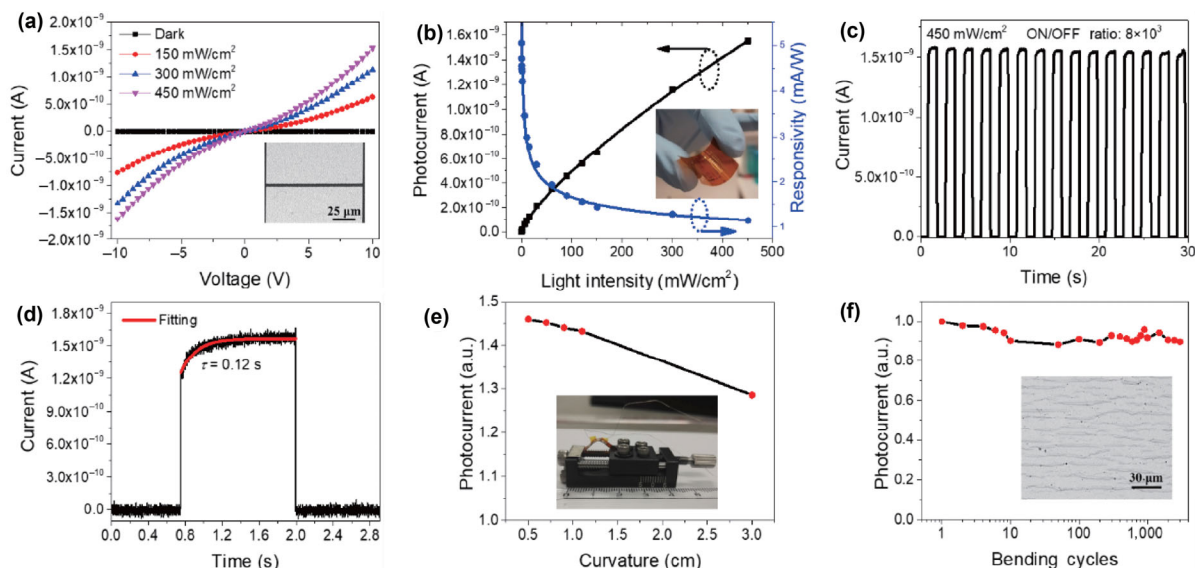

Figure 6 Mechanically flexible photodetectors based on monolayer WS$_2$. (a) Current–voltage curves under different light intensities. Inset: SEM image of a typical flexible photodetector with a channel length of 2 µm. (b) Photocurrent and responsivity vs. light intensity. Inset: optical image of a representative flexible photodetector. (c) Current vs. time plot measured under chopped light illumination with a light intensity of 450 mW/cm^2. (d) Current vs. time plot used to determine the rise and decay time constants. (e) Normalized photocurrent vs. bending curvature. Inset: optical image of flexible photodetector under bending. (f) Normalized photocurrent vs. bending cycles. Inset: SEM image of the device electrode after 3,000 bending cycles. The device used for the bending tests had a channel length of 83 µm.

is also plotted as a function of the light intensity in Fig. 6(b). Unlike the nearly linear relation between photocurrent and light intensity in WS$_2$ detectors configured on rigid sapphire, discussed before (Fig. 5(d)), a sub-linear relation is observed in this case, and the fitted value of β according to Eq. (1) is 0.756. A sub-linear dependence on the light intensity is always observed in photoconductive detectors [54–56] and is normally considered to be the result of complex processes such as electron–hole generation, trapping, and recombination in the semiconductor [57–59]. In the present case, defects may be generated during the transfer process of monolayer WS$_2$ from the grown sapphire substrate to the PI sheet, and they can then act as traps and recombination centers for photogenerated carriers, leading to sub-linear light intensity dependence in the photodetector. At the same time, the responsivity also varies with the light intensity, reaching a largest value of 5 mA/W, which is 10 times larger than that of the device fabricated on sapphire. A similar phenomenon was also observed for 2D GaS based photodetectors, which exhibit a higher photoresponsivity on flexible substrates [60]. The enhanced photoresponsivity observed in this study can be attributed to the relatively rough surface of PI substrates (Fig. S4 in the ESM), which can scatter the incident light, leading to the enhanced light absorption in monolayer WS$_2$. In addition, defects formed during the transfer may act as carrier traps, reducing the recombination probability of photo-generated carriers, thus increasing the photoresponsivity of the flexible photodetector. In addition, the flexible photodetector shows a higher specific detectivity compared with the photodetector configured on sapphire (Fig. S3(b) in the ESM). The maximum detectivity is measured as 4.0×10^{10} Jones at the light intensity of 0.07 mW/cm^2. Figure 6(c) displays a current vs. time plot under chopped light illumination, showing a clear on–off behavior with good stability. The on/off current ratio is found to be as high as 8×10^3, highlighting the good sensitivity of the photodetector. Moreover, the high-resolution current–time curve in Fig. 6(d) shows that the current exhibits an initial sharp rise followed by a slower increase. This phenomenon is often reported in nanomaterial-based photodetectors, where it can be attributed to the traps

and defects present in the bulk or on the surface of the material [61–63]. In short, as the photogenerated carriers would first fill the traps, the photocurrent would only reach a maximum after all traps are occupied, which delays the attainment of the steady state value [61]. This behavior is also consistent with the sub-linear dependence of the photocurrent on the light intensity. It is worth mentioning that the sharp rise exceeds the resolution of our equipment, which is lower than 560 µs. The slow rise can be fitted by an exponential decay function exp($-t/\tau$), where t is the time and τ is the time constant. The fitting yields $\tau = 0.12$ s, which represent the time constant of the slow-rise portion of the curve. On the other hand, after the illumination is switched off, the current decay is very fast, again exceeding the resolution of the equipment. This very fast decay indicates that the trapped charges can be released in a very efficient manner.

The device durability is another important require-ment for practical applications of flexible photodetectors. In order to determine the device stability during mechanical bending, photodetectors with large-size electrodes were fabricated to facilitate the measure-ments. A schematic illustration and an optical image of the measurement setup are shown in Figs. S5(a) and S5(b) in the ESM, respectively. For simplicity, the photocurrent is normalized to the case where no mechanical bending is performed. In this way, the normalized photocurrent can be easily measured as a function of the bending curvature (i.e., bending radius), as depicted in Fig. 6(e). Surprisingly, the photocurrent is found to increase with decreasing bending radius, which is unusual compared with other conventional 2D materials [64, 65]. Theoretical investigations reported that the band gap of monolayer WS$_2$ decreased when tensile stress is applied [66, 67]. The narrower band gap would result in a corresponding red shift in the absorption spectrum, contributing to the enhanced absorption under 532 nm light and improving the internal quantum efficiency of the fabricated photo-detector. At the same time, the tensile stress may also lead to the formation of structural defects, which can act as traps. Trapping of photogenerated carriers reduces their recombination probability, thus leading to enhanced photocurrent. In fact, an increase in photocurrent has also been observed in monolayer

MoS_2-based flexible photodetectors under mechanical bending, in perfect agreement with our present findings [68]. Moreover, to assess the device durability we evaluated the stability of the photocurrent as a function of the number of bending cycles. Remarkably, the photocurrent stays relatively stable, maintaining 89% of its initial value even after 3,000 bending cycles (Fig. 6(f) and Fig. S5(c) in the ESM). The slight photocurrent degradation can be probably attributed to the formation of wrinkles on the device electrodes and the subsequent increase in their contact resistance after the bending cycles, as displayed in the SEM image in the inset of Fig. 6(f). In any case, after the bending test, the photocurrent is still observed to increase with increasing tensile stress (Fig. S5(d) in the ESM). These results clearly demonstrate the mechanical flexibility and robustness of the wafer-scale, uniform, CVD-grown WS_2 monolayers for high-performance flexible optoelectronics. The present method can also be extended to the synthesis of wafer-scale monolayer MoS_2, as shown in Fig. S6 in the ESM, further illustrating its potential applicability to the synthesis of other 2D materials.

4 Conclusions

In summary, the wafer-scale synthesis of crystalline and homogenous WS_2 monolayers was successfully achieved using an enhanced CVD technique, in which precise control of different precursor vapor pressures was effectively established in a multi-temperature-zone horizontal tube furnace. Although transistors fabricated from the monolayer WS_2 films exhibit relatively low electron mobility, their mobility values can be improved by appropriate surface passivation to alleviate surface-adsorbed molecules and trapped charges. Importantly, once configured into photo-detectors on rigid substrates, the present monolayer WS_2 films display excellent response speeds (i.e., rise and decay time constants both shorter than 560 μs) and a respectable on/off current ratio of 5.5×10^3. Furthermore, when the monolayer WS_2 is integrated with flexible substrates, the resulting device displays an enhanced photoresponse with a responsivity of up to 5 mA/W, and the photocurrent is found to increase with decreasing bending radius, which can

be attributed to the reduction of the band gap under tensile stress. Notably, the photocurrent remains rather stable, with a degradation of only 11% even after 3,000 bending cycles. Overall, these results highlight the technological potential of the wafer-scale uniform monolayer WS_2 films developed in this work for practical applications in next-generation high-performance optoelectronics.

References

[1] Li, X. M.; Tao, L.; Chen, Z. F.; Fang, H.; Li, X. S.; Wang, X. R.; Xu, J.-B.; Zhu, H. W. Graphene and related two-dimensional materials: Structure-property relationships for electronics and optoelectronics. *Appl. Phys. Rev.* **2017**, *4*, 021306.

[2] Tan, C. L.; Cao, X. H.; Wu, X.-J.; He, Q. Y.; Yang, J.; Zhang, X.; Chen, J. Z.; Zhao, W.; Han, S. K.; Nam, G.-H. et al. Recent advances in ultrathin two-dimensional nano-materials. *Chem. Rev.* **2017**, *117*, 6225–6331.

[3] Chhowalla, M.; Jena, D.; Zhang, H. Two-dimensional semiconductors for transistors. *Nat. Rev. Mater.* **2016**, *1*, 16052.

[4] Xu, M. S.; Liang, T.; Shi, M. M.; Chen, H. Z. Graphene-like two-dimensional materials. *Chem. Rev.* **2013**, *113*, 3766–3798.

[5] Novoselov, K. S. Nobel lecture: Graphene: Materials in the flatland. *Rev. Mod. Phys.* **2011**, *83*, 837–849.

[6] Wang, Q. H.; Kalantar-Zadeh, K.; Kis, A.; Coleman, J. N.; Strano, M. S. Electronics and optoelectronics of two-dimensional transition metal dichalcogenides. *Nat. Nanotechnol.* **2012**, *7*, 699–712.

[7] Duan, X. D.; Wang, C.; Pan, A. L.; Yu, R. Q.; Duan, X. F. Two-dimensional transition metal dichalcogenides as atomically thin semiconductors: Opportunities and challenges. *Chem. Soc. Rev.* **2015**, *44*, 8859–8876.

[8] Liu, B. L.; Abbas, A.; Zhou, C. W. Two-dimensional semiconductors: From materials preparation to electronic applications. *Adv. Electron. Mater.* **2017**, *3*, 1700045.

[9] Mak, K. F.; Shan, J. Photonics and optoelectronics of 2D semiconductor transition metal dichalcogenides. *Nat. Photonics* **2016**, *10*, 216–226.

[10] Wang, H. T.; Yuan, H. T.; Hong, S. S.; Li, Y. B.; Cui, Y. Physical and chemical tuning of two-dimensional transition metal dichalcogenides. *Chem. Soc. Rev.* **2015**, *44*, 2664–2680.

[11] Bernardi, M.; Palummo, M.; Grossman, J. C. Extraordinary sunlight absorption and one nanometer thick photovoltaics using two-dimensional monolayer materials. *Nano Lett.* **2013**, *13*, 3664–3670.

[12] Yun, W. S.; Han, S. W.; Hong, S. C.; Kim, I. G.; Lee, J. D. Thickness and strain effects on electronic structures of transition metal dichalcogenides: 2H-MX$_2$ semiconductors (M = Mo, W; X = S, Se, Te). *Phys. Rev. B* **2012**, *85*, 033305.

[13] Hanbicki, A. T.; Currie, M.; Kioseoglou, G.; Friedman, A. L.; Jonker, B. T. Measurement of high exciton binding energy in the monolayer transition-metal dichalcogenides WS$_2$ and WSe$_2$. *Solid State Commun.* **2015**, *203*, 16–20.

[14] Zhu, B. R.; Chen, X.; Cui, X. D. Exciton binding energy of monolayer WS$_2$. *Sci. Rep.* **2015**, *5*, 9218.

[15] Zhang, W. X.; Huang, Z. S.; Zhang, W. L.; Li, Y. R. Two-dimensional semiconductors with possible high room temperature mobility. *Nano Res.* **2014**, *7*, 1731–1737.

[16] Akinwande, D.; Petrone, N.; Hone, J. Two-dimensional flexible nanoelectronics. *Nat. Commun.* **2014**, *5*, 5678.

[17] Chang, H.-Y.; Yang, S. X.; Lee, J.; Tao, L.; Hwang, W.-S.; Jena, D.; Lu, N. S.; Akinwande, D. High-performance, highly bendable MoS$_2$ transistors with high-k dielectrics for flexible low-power systems. *ACS Nano* **2013**, *7*, 5446–5452.

[18] Pu, J.; Funahashi, K.; Chen, C. H.; Li, M. Y.; Li, L. J.; Takenobu, T. Highly flexible and high-performance complementary inverters of large-area transition metal dichalcogenide monolayers. *Adv. Mater.* **2016**, *28*, 4111–4119.

[19] Lim, Y. R.; Song, W.; Han, J. K.; Lee, Y. B.; Kim, S. J.; Myung, S.; Lee, S. S.; An, K. S.; Choi, C. J.; Lim, J. Wafer-scale, homogeneous MoS$_2$ layers on plastic substrates for flexible visible-light photodetectors. *Adv. Mater.* **2016**, *28*, 5025–5030.

[20] Novoselov, K. S.; Jiang, D.; Schedin, F.; Booth, T. J.; Khotkevich, V. V.; Morozov, S. V.; Geim, A. K. Two-dimensional atomic crystals. *Proc. Natl. Acad. Sci. USA* **2005**, *102*, 10451–10453.

[21] Mak, K. F.; McGill, K. L.; Park, J.; McEuen, P. L. The valley Hall effect in MoS$_2$ transistors. *Science* **2014**, *344*, 1489–1492.

[22] Novoselov, K. S.; Geim, A. K.; Morozov, S. V.; Jiang, D.; Zhang, Y.; Dubonos, S. V.; Grigorieva, I. V.; Firsov, A. A. Electric field effect in atomically thin carbon films. *Science* **2004**, *306*, 666–669.

[23] Mattevi, C.; Kim, H.; Chhowalla, M. A review of chemical vapour deposition of graphene on copper. *J. Mater. Chem.* **2011**, *21*, 3324–3334.

[24] Kapolnek, D.; Wu, X. H.; Heying, B.; Keller, S.; Keller, B. P.; Mishra, U. K.; DenBaars, S. P.; Speck, J. S. Structural evolution in epitaxial metalorganic chemical vapor deposition grown GaN films on sapphire. *Appl. Phys. Lett.* **1995**, *67*, 1541–1543.

[25] Yu, Y. F.; Li, C.; Liu, Y.; Su, L. Q.; Zhang, Y.; Cao, L. Y. Controlled scalable synthesis of uniform, high-quality monolayer and few-layer MoS$_2$ films. *Sci. Rep.* **2013**, *3*, 1866.

[26] Gao, Y.; Liu, Z. B.; Sun, D.-M.; Huang, L.; Ma, L.-P.; Yin, L.-C.; Ma, T.; Zhang, Z.; Ma, X.-L.; Peng, L.-M. et al. Large-area synthesis of high-quality and uniform monolayer WS$_2$ on reusable Au foils. *Nat. Commun.* **2015**, *6*, 8569.

[27] Yun, S. J.; Chae, S. H.; Kim, H.; Park, J. C.; Park, J.-H.; Han, G. H.; Lee, J. S.; Kim, S. M.; Oh, H. M.; Seok, J. et al. Synthesis of centimeter-scale monolayer tungsten disulfide film on gold foils. *ACS Nano* **2015**, *9*, 5510–5519.

[28] Peimyoo, N.; Shang, J. Z.; Cong, C. X.; Shen, X. N.; Wu, X. Y.; Yeow, E. K. L.; Yu, T. Nonblinking, intense two-dimensional light emitter: Monolayer WS$_2$ triangles. *ACS Nano* **2013**, *7*, 10985–10994.

[29] Zhang, Y.; Zhang, Y. F.; Ji, Q. Q.; Ju, J.; Yuan, H. T.; Shi, J. P.; Gao, T.; Ma, D. L.; Liu, M. X.; Chen, Y. B. et al. Controlled growth of high-quality monolayer WS$_2$ layers on sapphire and imaging its grain boundary. *ACS Nano* **2013**, *7*, 8963–8971.

[30] Cong, C. X.; Shang, J. Z.; Wu, X.; Cao, B. C.; Peimyoo, N.; Qiu, C. Y.; Sun, L. T.; Yu, T. Synthesis and optical properties of large-area single-crystalline 2D semiconductor WS$_2$ monolayer from chemical vapor deposition. *Adv. Optical*

Mater. **2014**, *2*, 131–136.

[31] Li, S. S.; Wang, S. F.; Tang, D.-M.; Zhao, W. J.; Xu, H. L.; Chu, L. Q.; Bando, Y.; Golberg, D.; Eda, G. Halide-assisted atmospheric pressure growth of large WSe_2 and WS_2 monolayer crystals. *Appl. Mater. Today* **2015**, *1*, 60–66.

[32] Lan, C. Y.; Li, C.; Yin, Y.; Liu, Y. Large-area synthesis of monolayer WS_2 and its ambient-sensitive photo-detecting performance. *Nanoscale* **2015**, *7*, 5974–5980.

[33] Jiang, X. C.; Xiong, Q. H.; Nam, S.; Qian, F.; Li, Y.; Lieber, C. M. InAs/InP radial nanowire heterostructures as high electron mobility devices. *Nano Lett.* **2007**, *7*, 3214–3218.

[34] Ford, A. C.; Ho, J. C.; Fan, Z. Y.; Ergen, O.; Altoe, V.; Aloni, S.; Razavi, H.; Javey, A. Synthesis, contact printing, and device characterization of Ni-catalyzed, crystalline InAs nanowires. *Nano Res.* **2008**, *1*, 32–39.

[35] Gurarslan, A.; Yu, Y. F.; Su, L. Q.; Yu, Y. L.; Suarez, F.; Yao, S. S.; Zhu, Y.; Ozturk, M.; Zhang, Y.; Cao, L. Y. Surface-energy-assisted perfect transfer of centimeter-scale monolayer and few-layer MoS_2 films onto arbitrary substrates. *ACS Nano* **2014**, *8*, 11522–11528.

[36] Benameur, M. M.; Radisavljevic, B.; Héron, J. S.; Sahoo, S.; Berger, H.; Kis, A. Visibility of dichalcogenide nanolayers. *Nanotechnology* **2011**, *22*, 125706.

[37] Zhang, X.; Qiao, X.-F.; Shi, W.; Wu, J.-B.; Jiang, D.-S.; Tan, P.-H. Phonon and Raman scattering of two-dimensional transition metal dichalcogenides from monolayer, multilayer to bulk material. *Chem. Soc. Rev.* **2015**, *44*, 2757–2785.

[38] McCreary, K. M.; Hanbicki, A. T.; Singh, S.; Kawakami, R. K.; Jernigan, G. G.; Ishigami, M.; Ng, A.; Brintlinger, T. H.; Stroud, R. M.; Jonker, B. T. The effect of preparation conditions on Raman and photoluminescence of monolayer WS_2. *Sci. Rep.* **2016**, *6*, 35154.

[39] Peimyoo, N.; Shang, J. Z.; Yang, W. H.; Wang, Y. L.; Cong, C. X.; Yu, T. Thermal conductivity determination of suspended mono- and bilayer WS_2 by Raman spectroscopy. *Nano Res.* **2015**, *8*, 1210–1221.

[40] Zhao, W. J.; Ghorannevis, Z.; Amara, K. K.; Pang, J. R.; Toh, M.; Zhang, X.; Kloc, C.; Tan, P. H.; Eda, G. Lattice dynamics in mono- and few-layer sheets of WS_2 and WSe_2. *Nanoscale* **2013**, *5*, 9677–9683.

[41] Zhao, W. J.; Ghorannevis, Z.; Chu, L. Q.; Toh, M.; Kloc, C.; Tan, P.-H.; Eda, G. Evolution of electronic structure in atomically thin sheets of WS_2 and WSe_2. *ACS Nano* **2013**, *7*, 791–797.

[42] Su, L. Q.; Yu, Y. F.; Cao, L. Y.; Zhang, Y. Effects of substrate type and material-substrate bonding on high-temperature behavior of monolayer WS_2. *Nano Res.* **2015**, *8*, 2686–2697.

[43] Kim, W.; Javey, A.; Vermesh, O.; Wang, Q.; Li, Y. M.; Dai, H. J. Hysteresis caused by water molecules in carbon nanotube field-effect transistors. *Nano Lett.* **2003**, *3*, 193–198.

[44] Park, Y.; Baac, H. W.; Heo, J.; Yoo, G. Thermally activated trap charges responsible for hysteresis in multilayer MoS_2 field-effect transistors. *Appl. Phys. Lett.* **2016**, *108*, 083102.

[45] Qiu, H.; Pan, L. J.; Yao, Z. N.; Li, J. J.; Shi, Y.; Wang, X. R. Electrical characterization of back-gated bi-layer MoS_2 field-effect transistors and the effect of ambient on their performances. *Appl. Phys. Lett.* **2012**, *100*, 123104.

[46] Ghatak, S.; Pal, A. N.; Ghosh, A. Nature of electronic states in atomically thin MoS_2 field-effect transistors. *ACS Nano* **2011**, *5*, 7707–7712.

[47] Li, S.-L.; Wakabayashi, K.; Xu, Y.; Nakaharai, S.; Komatsu, K.; Li, W.-W.; Lin, Y.-F.; Aparecido-Ferreira, A.; Tsukagoshi, K. Thickness-dependent interfacial coulomb scattering in atomically thin field-effect transistors. *Nano Lett.* **2013**, *13*, 3546–3552.

[48] Lee, Y.; Lee, J.; Bark, H.; Oh, I.-K.; Ryu, G. H.; Lee, Z.; Kim, H.; Cho, J. H.; Ahn, J.-H.; Lee, C. Synthesis of wafer-scale uniform molybdenum disulfide films with control over the layer number using a gas phase sulfur precursor. *Nanoscale* **2014**, *6*, 2821–2826.

[49] Lee, Y. H.; Zhang, X. Q.; Zhang, W. J.; Chang, M. T.; Lin, C. T.; Chang, K. D.; Yu, Y. C.; Wang, J. T. W.; Chang, C. S.; Li, L. J. et al. Synthesis of large-area MoS_2 atomic layers with chemical vapor deposition. *Adv. Mater.* **2012**, *24*, 2320–2325.

[50] Liu, K.-K.; Zhang, W. J.; Lee, Y.-H.; Lin, Y.-C.; Chang, M.-T.; Su, C.-Y.; Chang, C.-S.; Li, H.; Shi, Y. M.; Zhang, H. et al. Growth of large-area and highly crystalline MoS_2 thin layers on insulating substrates. *Nano Lett.* **2012**, *12*, 1538–1544.

[51] Perea-López, N.; Elías, A. L.; Berkdemir, A.; Castro-Beltran, A.; Gutiérrez, H. R.; Feng, S. M.; Lv, R. T.; Hayashi, T.; López-Urías, F.; Ghosh, S. et al. Photosensor device based on few-layered WS_2 films. *Adv. Funct. Mater.* **2013**, *23*, 5511–5517.

[52] Pawbake, A. S.; Waykar, R. G.; Late, D. J.; Jadkar, S. R. Highly transparent wafer-scale synthesis of crystalline WS_2 nanoparticle thin film for photodetector and humidity-sensing applications. *ACS Appl. Mater. Interfaces* **2016**, *8*, 3359–3365.

[53] Yao, J. D.; Zheng, Z. Q.; Shao, J. M.; Yang, G. W. Stable, highly-responsive and broadband photodetection based on large-area multilayered WS_2 films grown by pulsed-laser deposition. *Nanoscale* **2015**, *7*, 14974–14981.

[54] Guo, N.; Hu, W. D.; Liao, L.; Yip, S.; Ho, J. C.; Miao, J. S.; Zhang, Z.; Zou, J.; Jiang, T.; Wu, S. W. et al. Anomalous and highly efficient InAs nanowire phototransistors based

on majority carrier transport at room temperature. *Adv. Mater.* **2014**, *26*, 8203–8209.

[55] Lan, C. Y.; Li, C.; Yin, Y.; Guo, H. Y.; Wang, S. Synthesis of single-crystalline GeS nanoribbons for high sensitivity visible-light photodetectors. *J. Mater. Chem. C* **2015**, *3*, 8074–8079.

[56] Lan, C. Y.; Li, C.; Wang, S.; He, T. Y.; Zhou, Z. F.; Wei, D. P.; Guo, H. Y.; Yang, H.; Liu, Y. Highly responsive and broadband photodetectors based on WS_2–graphene van der Waals epitaxial heterostructures. *J. Mater. Chem. C* **2017**, *5*, 1494–1500.

[57] Binet, F.; Duboz, J. Y.; Rosencher, E.; Scholz, F.; Härle, V. Mechanisms of recombination in GaN photodetectors. *Appl. Phys. Lett.* **1996**, *69*, 1202–1204.

[58] Chen, R.-S.; Chen, H.-Y.; Lu, C.-Y.; Chen, K.-H.; Chen, C.-P.; Chen, L.-C.; Yang, Y.-J. Ultrahigh photocurrent gain in *m*-axial GaN nanowires. *Appl. Phys. Lett.* **2007**, *91*, 223106.

[59] Soci, C.; Zhang, A.; Xiang, B.; Dayeh, S. A.; Aplin, D. P. R.; Park, J.; Bao, X. Y.; Lo, Y.-H.; Wang, D. ZnO nanowire UV photodetectors with high internal gain. *Nano Lett.* **2007**, *7*, 1003–1009.

[60] Hu, P. A.; Wang, L. F.; Yoon, M.; Zhang, J.; Feng, W.; Wang, X. N.; Wen, Z. Z.; Idrobo, J. C.; Miyamoto, Y.; Geohegan, D. B. et al. Highly responsive ultrathin GaS nanosheet photodetectors on rigid and flexible substrates. *Nano Lett.* **2013**, *13*, 1649–1654.

[61] Jiang, Y.; Zhang, W. J.; Jie, J. S.; Meng, X. M.; Fan, X.; Lee, S. T. Photoresponse properties of CdSe single-nanoribbon photodetectors. *Adv. Funct. Mater.* **2007**, *17*, 1795–1800.

[62] Cunningham, G.; Khan, U.; Backes, C.; Hanlon, D.; McCloskey, D.; Donegan, J. F.; Coleman, J. N. Photoconductivity of solution-processed MoS_2 films. *J. Mater. Chem. C* **2013**, *1*, 6899–6904.

[63] Zhou, X.; Zhang, Q.; Gan, L.; Li, H. Q.; Zhai, T. Y. Large-size growth of ultrathin SnS_2 nanosheets and high performance for phototransistors. *Adv. Funct. Mater.* **2016**, *26*, 4405–4413.

[64] Zhou, Y. B.; Nie, Y. F.; Liu, Y. J.; Yan, K.; Hong, J. H.; Jin, C. H.; Zhou, Y.; Yin, J. B.; Liu, Z. F.; Peng, H. L. Epitaxy and photoresponse of two-dimensional GaSe crystals on flexible transparent mica sheets. *ACS Nano* **2014**, *8*, 1485–1490.

[65] Zheng, Z. Q.; Zhang, T. M.; Yao, J. D.; Zhang, Y.; Xu, J. R.; Yang, G. W. Flexible, transparent and ultra-broadband photodetector based on large-area WSe_2 film for wearable devices. *Nanotechnology* **2016**, *27*, 225501.

[66] Ghorbani-Asl, M.; Borini, S.; Kuc, A.; Heine, T. Strain-dependent modulation of conductivity in single-layer transition-metal dichalcogenides. *Phys. Rev. B* **2013**, *87*, 235434.

[67] Wang, Y. L.; Cong, C. X.; Yang, W. H.; Shang, J. Z.; Peimyoo, N.; Chen, Y.; Kang, J. Y.; Wang, J. P.; Huang, W.; Yu, T. Strain-induced direct–indirect bandgap transition and phonon modulation in monolayer WS_2. *Nano Res.* **2015**, *8*, 2562–2572.

[68] De Fazio, D.; Goykhman, I.; Yoon, D.; Bruna, M.; Eiden, A.; Milana, S.; Sassi, U.; Barbone, M.; Dumcenco, D.; Marinov, K. et al. High responsivity, large-area graphene/MoS_2 flexible photodetectors. *ACS Nano* **2016**, *10*, 8252–8262.